

Article

Photoluminescence Enhancement and Carrier Dynamics of Charged Biexciton in Monolayer WS₂ Coupled with Plasmonic Nanocavity

Huiqiang Geng ¹, Qirui Liu ¹, Yuxiang Tang ² and Ke Wei ^{1,*}

¹ College of Advanced Interdisciplinary Studies, National University of Defense Technology, Changsha 410073, China; genghuiqiang@nudt.edu.cn (H.G.); lqrkili@163.com (Q.L.)

² Institute for Quantum Science and Technology, National University of Defense Technology, Changsha 410073, China; yxtang@nudt.edu.cn

* Correspondence: weikeap@163.com

Abstract: Monolayer two-dimensional transition metal dichalcogenide (TMD)-based materials have become one of the ideal platforms for the study of multibody interactions due to their rich excitonic complexes. The coupling between optical nanocavity and material has become an important means for manipulating the optical properties of materials, but there are few studies on the coupling of nanocavities and the multi-body effect in materials. In this study, we investigate the optical properties of silver nanodisk (Ag ND) arrays covering a monolayer WS₂. In the experimental sample, we observed a ~114.3-fold photoluminescence enhancement of charged biexciton in the heterostructure region, as compared to the monolayer WS₂ region, a value which is much higher than those for exciton (~2.2-fold) and trion (~16.4-fold), a finding which is attributed to the Fano resonant coupling between monolayer WS₂ and the Ag ND. By means of time-resolved spectroscopy, we studied the carrier dynamics in the hybrid system. Our findings reveal that resonant coupling promotes the formation and radiation recombination processes of the charged biexciton, significantly reducing the radiative recombination lifetime by ~15-fold, which is much higher than the measurement in exciton (~2-fold). Our results provide an opportunity to understand the multibody physics of coupling with nanocavities, which could facilitate the application of multi-body excitons in the fields of light-emitting devices and lasers, etc.



Citation: Geng, H.; Liu, Q.; Tang, Y.; Wei, K. Photoluminescence Enhancement and Carrier Dynamics of Charged Biexciton in Monolayer WS₂ Coupled with Plasmonic Nanocavity. *Photonics* **2024**, *11*, 358. <https://doi.org/10.3390/photonics11040358>

Received: 21 March 2024

Revised: 3 April 2024

Accepted: 10 April 2024

Published: 12 April 2024



Copyright: © 2024 by the authors. Licensee MDPI, Basel, Switzerland. This article is an open access article distributed under the terms and conditions of the Creative Commons Attribution (CC BY) license (<https://creativecommons.org/licenses/by/4.0/>).

Keywords: transition metal dichalcogenides; charged biexciton; Fano; plasmon; carrier dynamics

1. Introduction

In recent years, monolayer two-dimensional transition metal dichalcogenide (TMD)-based materials have received extensive attention due to their excellent photoelectronic properties [1,2]. Compared with bulk materials, monolayer TMD-based materials exhibit reduced dielectric screening and enhanced Coulomb interactions, leading to the generation of excitons, which are quasiparticles consisting of electron-hole pairs with binding energies of hundreds of meV [3]. The tightly bound exciton offers an ideal platform for the investigation of many-body physics [4,5]. In the last few years, multibody excitonic complexes, such as trion, a three-particle state consisting of one hole and two electrons; biexciton, a four-particle state consisting of two holes and two electrons; and charged biexciton, a five-particle state consisting of two holes and three electrons, have been identified [6–8]. Owing to the important application prospects of charged biexciton in entangled photon sources [9], the study and manipulation of charged biexciton emission in TMDs have important implications for the fabrication of advanced photonics and optoelectronic devices.

The coupling between plasmonic nanocavities and TMD-based materials has been demonstrated as an effective means to enhance the emission properties of TMDs [10–13]. This enhancement can be analyzed in two ways. Firstly, the presence of metal structures in

close proximity can increase the local density of photonic states in plasmonic nanostructures [14,15]. This can result in a shortened fluorescence lifetime and significant inhibition of Auger recombination [16]. Secondly, while the exciton state in TMD-based materials is discrete, the plasmons are considered to be continuous energy states due to the large linewidth broadening. The interaction between these continuous and discrete energy states leads to the well-known Fano effect, in which energy is transferred to enhance the photoluminescence of the emitter [17–19]. While there have been numerous studies on the coupling of plasmonic nanocavities with TMD-based materials [20,21], significant research has also been conducted on ultrafast optics-based interactions between plasmons and materials [22–24]. However, there are still deficiencies in understanding the multibody effect and the coupling of nanocavities associated with charged biexciton of monolayer TMDs, especially the strong charged biexciton emissions and the ultrafast carrier dynamics in this hybrid system. Hence, it is crucial to amplify the emission of charged biexciton through the utilization of the plasmonic nanocavity. Furthermore, comprehending the enhancement of plasmon coupling within these metal nanostructure-incorporated TMD-based systems is pivotal, as it will facilitate the advancement of photoelectric devices reliant on charged biexciton in TMDs.

In this article, we study the optical characteristics of the monolayer WS₂ coupled with plasmonic nanocavity by means of steady-state and time-resolved spectroscopy. Specifically, we demonstrate the observation of charged biexciton by using steady-state power-dependent photoluminescence (PL) spectroscopy. It is determined that the charged biexciton shows a giant enhancement in emission (~114.3-fold), compared with exciton (~2.2-fold) and trion (~16.4-fold), which is attributed to the Fano resonant coupling of monolayer WS₂ and the Ag ND. Subsequently, with the help of femtosecond pump-probe measurements, it is proved that Fano resonance coupling promotes the formation and radiative recombination processes of exciton, trion, and charged biexciton. The effect of the plasmonics on the radiative recombination lifetime of charged biexciton is much stronger than that seen with exciton. Our work not only provides a method for the formation and utilization of charged biexciton in TMD-based materials, but also establishes a way to understand the coupling of higher-order exciton states in TMD-based materials and plasmonic nanocavities through the analysis of carrier dynamics.

2. Materials and Methods

Figure 1a illustrates the structure of the sample, which was fabricated as follows: a monolayer of WS₂ film was synthesized using the chemical vapor deposition (CVD) method and transferred onto a pre-prepared quartz substrate via the wet transfer technique. Then electron beam lithography and evaporation and stripping technology were used to grow a 30 nm thick silver nanodisk (Ag ND) array. Finally, to prevent sample degradation, a 200 nm thick polymethyl methacrylate (PMMA) coating was applied for encapsulation. Figure 1b depicts the scanning electron microscope. The period of the Ag ND array is fixed at 300 nm, while the array diameter is ~110 nm. Figure 1c shows the optical microscopy images of the WS₂–Ag ND sample. The lack of uniformity in the WS₂ layer below the plasmonic structures could be attributed to the presence of multi-layer regions during the growth of the WS₂ layer in the CVD process. However, overall, the sample growth exhibits a high degree of uniformity.

The optical test system used in the experiment is shown in Figure 2. In this experimental setup, the pump pulse pre-irradiates the sample, immediately triggering various excited states, including plasmon, exciton, and their coupling system. The reflectance R_0 of the subsequent probe pulse is influenced by these pump-induced excited states. This white probe light is then focused onto the sample using a microscope, with a beam diameter of approximately 1.5 μm (width of 1/e intensity). Additionally, the dynamics of the excited states are characterized by adjusting the time delay between the two light pulses using a delay line, achieving a time resolution of approximately 200 fs, as defined by the pulse width of the combined beams. The dynamics of the excited states are monitored

by varying the time delay (t) between the two pulses using a delay line. The transient signal is recorded as a reflectance contrast, $\Delta R(t)/R_0 = (R(t) - R_0)/R_0$, where $R(t)$ and R_0 represent the probe reflectance with and without pumping. The optical signal undergoes spectral analysis, for which a grating spectrograph (Shamrock 500i, Oxford Instruments, London, UK) is used, and is then captured by a plane array CCD camera (iVac 316, Oxford Instruments). The time-correlated single photon counting (TCSPC) testing was conducted using PC-150NX TCSPC modules in conjunction with an HPM-100-07 (Oxford Instruments, London, UK) detector.

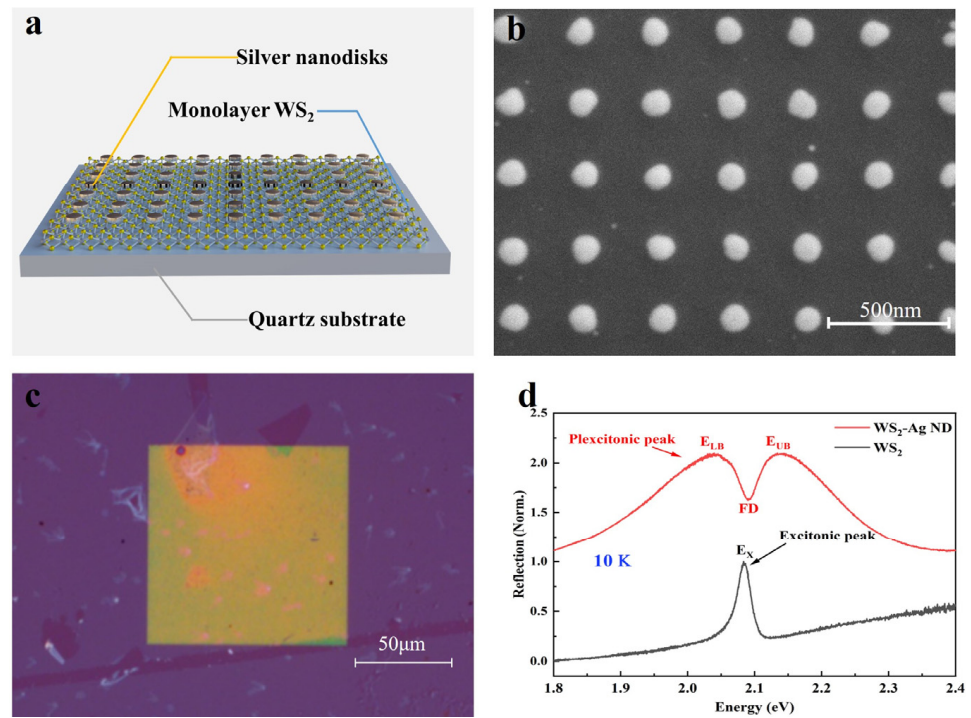


Figure 1. (a) Schematic diagram of the WS₂-Ag ND hybrid system. (b) Scanning electron microscope image. (c) Optical microscopy image of the WS₂-Ag ND heterostructure sample. (d) The reflectance spectra of monolayer WS₂ (black) and the WS₂-Ag ND heterostructure (red) at 10K temperature.

As shown in Figure 1d, the reflectance spectra of the sample in monolayer WS₂ and the WS₂-Ag ND heterostructure regions were tested at a temperature of 10K. The reflectance spectra are recorded as $R = (R_{\text{sample}} - R_{\text{substrate}})/R_{\text{substrate}}$, where R_{sample} and $R_{\text{substrate}}$ are the reflectances of the sample and the quartz substrate. When comparing the reflection spectra of monolayer WS₂ with those of the heterostructure region graphically, we observe that the heterostructure displays a pronounced Fano resonance dip (FD) around the exciton energy (E_x) in monolayer WS₂, and two peaks, on the left and right, which are defined as the low energy (LE) and upper energy (UE) branches. The comparable amplitude of LE and UE indicates that the plasmon resonates with the neutral exciton in monolayer WS₂, and thus energy can be efficiently transferred from the plasmon cavity to the exciton [20,25].

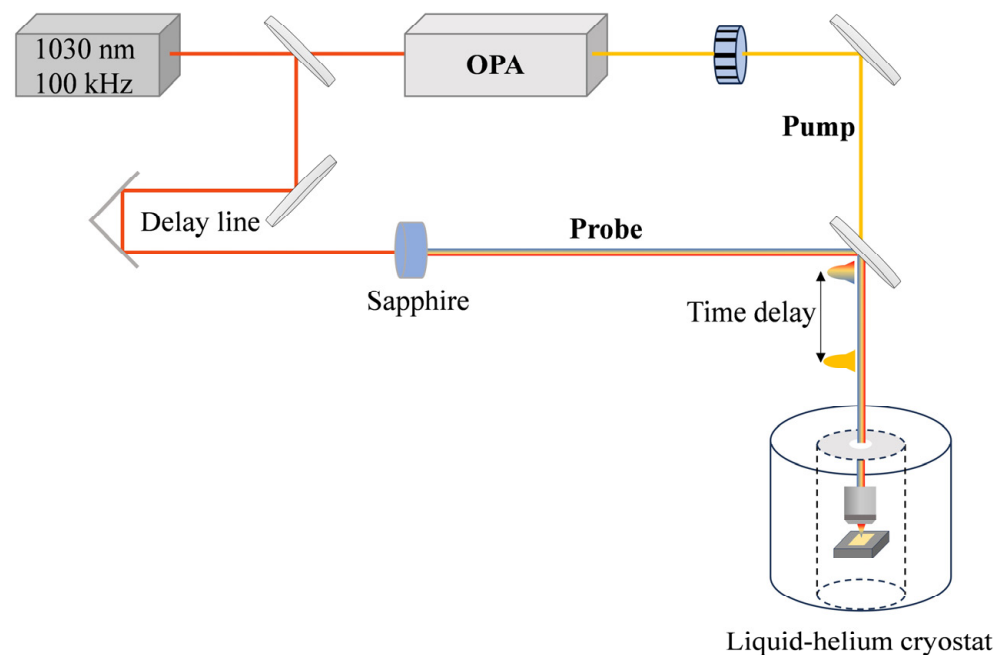


Figure 2. Schematic of the transient differential reflection (TR) measurement setup. The femtosecond light emitted by a Pharos femtosecond laser system (PH2–20W, Light Conversion, 1030 nm, 100 kHz, FWHM of 230 fs, and 20 W) is split into two beams. The stronger beam is directed to an optical parametric amplifier (ORPHEUS-HP, Light Conversion) to produce a wavelength-tunable pump beam with an FWHM of 140 fs. The weaker beam is focused on a high-quality sapphire crystal to generate a supercontinuum white light probe pulse. The cryogenic temperature is maintained by a liquid-helium exchange gas cryostat (attoDRY1000, Attocube systems AG) equipped with a confocal system with a numerical aperture of 0.82.

3. Results and Discussion

3.1. Steady-State Power-Dependent Photoluminescence (PL) Spectroscopy

To study the fluorescence characteristics of the sample, power-dependent PL tests were performed on both the pure monolayer WS_2 and the WS_2 -Ag ND heterostructure, excited by a 560 nm (~ 2.21 eV) laser at a temperature of 10K. Figure 3a shows the typical PL spectra under the 100 μW pump power. Four peaks were found in both of the two regions, among which the strong and broadband spectral peaks below 2 eV come from the emission of trap state excitons. These trap states may originate from lattice defects within the WS_2 itself or from doping by the overlying PPMA, serving as a substantial electron reservoir for the generation of charged excitonic states through the photogating effect [26]. Figure 3b shows the Voigt fitting curve of the intrinsic PL spectrum after the removal of the trap state PL, in which three peaks above 2 eV are obtained, labeled X (~ 2.090 eV), T (~ 2.063 eV), and XX^- (~ 2.040 eV). The energy differences between the X and the latter two peaks are 27 meV and 50 meV. According to a previous study [7], these peaks can be attributed to the emissions from exciton, trion, and charged biexciton. The pronounced PL emission peak signal not only indicates the suitability of our sample for facilitating the formation of multibody exciton states but also establishes a robust platform for investigating the coupling of multibody excitons with cavities.

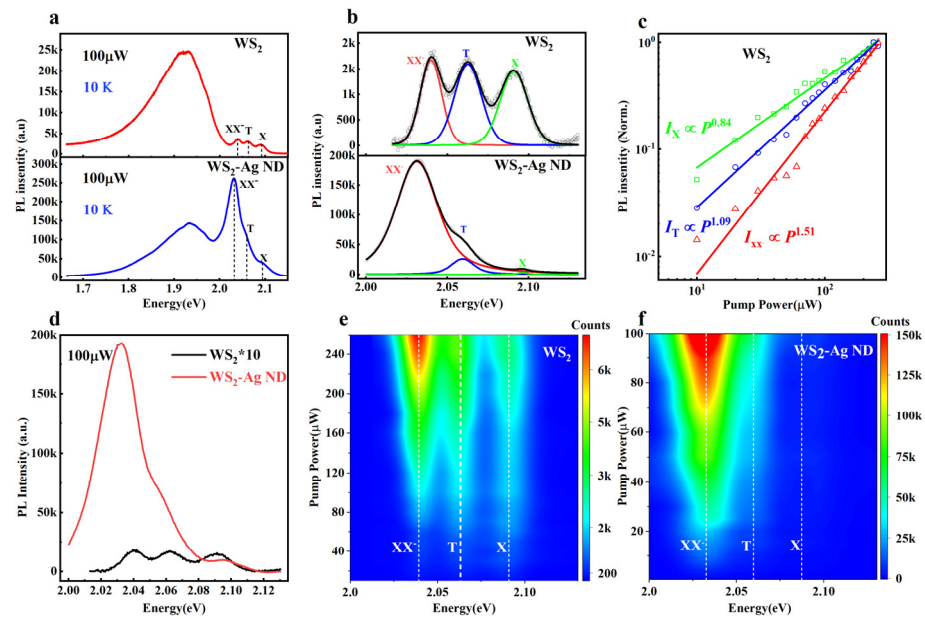


Figure 3. Power-dependent PL spectra of monolayer WS₂ at 10K excited by 560 nm laser. (a) Typical PL spectra of monolayer WS₂ and the WS₂-Ag ND heterostructure with an excitation power of 100 μW. (b) Voigt fitting curve of PL spectra in (a) after removing the trap state PL. (c) PL intensity as a function of the pump power at the X, T, and XX⁻ peaks in monolayer WS₂. (d) PL spectra comparison after removing the trap state PL. (e,f) Contour map of power-dependent PL spectra of monolayer WS₂ and the WS₂-Ag ND heterostructure after removing the trap state PL.

Figure 3c extracts the PL intensities of different excitonic complexes (I_X , I_T , and I_{XX^-}) as a function of the pump power P , fitting with the power-law model ($I \propto P^\alpha$). The fitting exponents of the X, T are 0.84 and 1.09, respectively, showing sublinear and linear power-dependent emission, indicating their single-particle characteristic. In contrast, the XX⁻ displays a distinctly superlinear behavior, with an α of 1.51, indicating its biexcitonic nature, which possibly arises from neutral biexciton or charged biexciton. The former, however, possesses a binding energy of 20–25 meV [7]; the comparison with neutral exciton, which falls significantly below the observed value of 50 meV here, eliminates the likelihood of its presence. To further study the effect of plasmonics on excitonic emission, Figure 3d compares the PL spectra from both sample regions on a shared coordinate system after removing the trap state PL. Compared with the pure WS₂, the three emission peaks in the heterostructure have been enhanced. Importantly, the enhancement of the XX⁻ is ~114.3-fold, which is much higher than those of X (~2.2-fold) and T (~16.4-fold). To the best of our knowledge, such a large PL enhancement of charged biexciton has not been observed in previous studies. Figure 2e,f further show the contour map of the power-dependent intrinsic PL spectra, which show that in the whole pump power range, the PL emission peaks in the heterostructure region are much higher than those in monolayer WS₂ region, and the emission peak is always dominated by XX⁻. In addition, the data fitting in Figure 3c is derived from Figure 3e,f. Throughout the entire range of pump power values, no variation in the linear coefficient α is observed. This absence of change suggests that our sample likely operates within a well-defined linear range, or the inability to test its nonlinearity under high-power working regime may stem from limitations in the testing conditions. The strong field around the plasmon cavity can penetrate the single atom layer thickness of WS₂. In principle, the enhancement of the plasmonic nanocavity can be caused by two factors: the enhancement from the excitonic generation, or the promotion of the excitonic emission. In the sample structure, the plasmonic nanocavity is directly attached to a single layer of WS₂ without a dielectric layer in the middle. Specifically, in the photo absorption process, the Fano resonance emerging between the plasmonic nanocavity and the monolayer WS₂ may lead to the energy transfer from Ag ND to WS₂, as the absorption coefficient of the former

is much larger than that of the latter. Additionally, during the recombination process, the plasmonic nanocavity may also enhance the radiative recombination process. As a result, the photoluminescence of the excitonic complexes undergoes significant enhancement.

However, the linear width of the plasmonic cavity is broad, and the range of formant can cover the whole resonance energy level of the excitonic complexes, which indicates that the enhanced PL emission caused by plasmon resonance is effective for exciton, trion, and charged biexciton. These explanations are insufficient to explain the finding that the fluorescence of charged double excitons in the heterogeneous region is significantly enhanced compared to those of exciton and trion, and the emission of charged biexciton is dominant. This phenomenon underscores the necessity for a more elaborate analysis of the impact of plasmonic nanocavities on monolayer WS₂. To conduct a more thorough analysis of the PL enhancement phenomenon predominantly influenced by charged biexciton in the heterogeneous region, the samples underwent testing and analysis using ultrafast optics technology. This method provides detailed information on the carrier dynamics of the samples, enabling a comprehensive analysis of the predominant PL enhancement mechanism of charged biexciton in heterostructure region.

3.2. Time-Resolved PL and Femtosecond Pump-Probe Measurements

In order to better understand why the charged biexciton produces such a giant PL enhancement in the heterostructure region, time-resolved PL of WS₂ and WS₂-Ag ND samples were investigated by using the time-correlated single photon counting (TCSPC) technique under 560 nm excitation, and the probe wavelength was focused at the XX⁻ resonance. As shown in Figure 4, the time-resolved PL can be fitted by double exponential decay:

$$I(t) = A_1 * e^{-\frac{t}{\tau_1}} + A_2 * e^{-\frac{t}{\tau_2}} \quad (1)$$

where $I(t)$ represents the change of normalized PL intensity with time, A_1 and A_2 represent the proportions of the two relaxation processes, and τ_1 and τ_2 represent the characteristic lifetimes of the two relaxation processes. Commonly, τ_1 can be attributed to the non-radiative recombination process, and τ_2 to the radiative one. It is noteworthy that at higher pump powers, the elevation in exciton density could potentially trigger exciton–exciton annihilation, thereby reducing the lifetime. However, for all pumping powers, both the τ_1 and the τ_2 in the heterostructure are smaller than those in the monolayer WS₂, which implies that PL relaxation is not affected by pumping-power-dependent exciton–exciton annihilation interaction [27]. This is also consistent with the previous analysis finding that the sample has a good linear operating range. In other words, the recombination rate is enhanced by the plasmonic nanocavity. The TCSPC analysis offers limited insights into the analysis of PL enhancement in heterogeneous regions from a recombination lifetime perspective.

Due to the limited time resolution of TCSPC, the effect of the plasmonic coupling on the exciton emission cannot be better analyzed. To further understand the formation and relaxation processes of charged biexciton induced by plasmons, the transient differential reflectance spectra were measured by femtosecond-pulsed laser pumping at 560 nm at 4K. To avoid the nonlinear effects induced by the high carrier density, a pump fluence of 10 $\mu\text{J cm}^{-2}$ was selected. Figure 5a,d show the pseudo-color diagram of the transient differential reflection spectra (ΔR) of controlled WS₂ and the heterostructure. For WS₂, three well-separated photoinduced bleaching (PB, red area) signals are clearly found, located at the X, T, and XX⁻ resonances in the first 1 ps; these are attributed to their state-filling effects [28]. In the heterostructure region, the three bleaching signals all convert to three photoinduced absorption (PA, blue area) peaks in an early time delay of <1 ps, which is the hallmark of the saturation nonlinear effects of the excitons, in which the Pauli blocking of the pump injecting exciton reduces the coupling strength between the excitons and plasmon [20,29]. In Figure 5b,e, the transient differential reflection spectra at selected probe delays showcase three clearly separated peaks and their temporal progression. The clearly separated peak signals detected under femtosecond pumping suggest that our

fabricated sample is highly conducive to investigating the interplay between multibody exciton states and nanocavity in TMDs materials. We can distinctly observe the temporal evolution of the three excitonic states in the sample from the time-resolved spectrum. To obtain more detailed information about the relaxation process, the differential reflection spectrum signals of the three PB peaks in WS₂ and the three PA peaks in the heterostructure region are dynamically fitted using the multi-exponential function outlined in Formula (2):

$$\Delta R = \Delta R_0 - a_0 * e^{\frac{t-t_0}{\tau_{rise}}} + a_1 * e^{-\frac{t-t_0}{\tau_1}} + a_2 * e^{-\frac{t-t_0}{\tau_2}} + a_3 * e^{-\frac{t-t_0}{\tau_3}} \quad (2)$$

where ΔR represents the differential reflection spectrum signal of the formant peak; ΔR_0 represents the base of the signal; t_0 represents the baseline at which the pump of the signal begins; a_0 and τ_{rise} represent the fitting coefficient and life of the signal during the rise process; $a_1, a_2,$ and $a_3,$ and $\tau_1, \tau_2,$ and τ_3 represent the exponential fitting coefficient and life of the signal during the decay process, with the relevant parameters listed in Table 1. The fitting results of three PB peaks of monolayer WS₂ and three PA peaks of the heterostructure region are shown in Figure 5c,f.

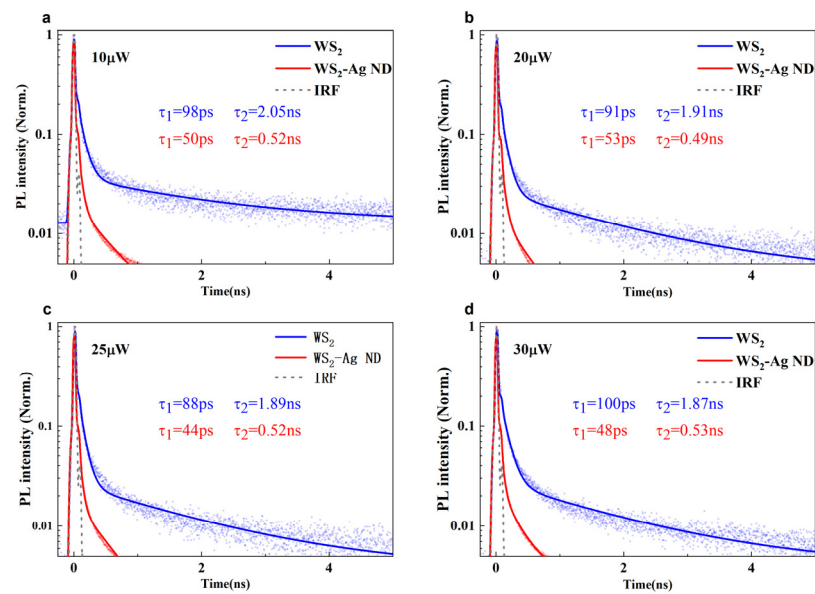


Figure 4. (a–d) Comparison of normalized PL decay from monolayer WS₂ (blue) and the WS₂-Ag ND heterostructure (red) samples, at 2.04 eV (XX⁻ resonance) under different levels of pump power. The gray lines stand for the instrumental response function (IRF), with a full width at half-maximum of ~20 ps.

Table 1. Fitting parameters of the time-resolved differential reflection signal.

	X		T		XX ⁻	
	WS ₂ (ps)	WS ₂ -Ag ND (ps)	WS ₂ (ps)	WS ₂ -Ag ND (ps)	WS ₂ (ps)	WS ₂ -Ag ND (ps)
τ _{rise}	0.27	0.09	0.27	0.24	0.16	0.10
τ ₁	6.60	0.09	0.29	0.27	0.56	0.17
τ ₂	64.49	0.62	2.81	1.14	3.71	3.32
τ ₃	211.84	131.45	N/A	N/A	292.94	20.10

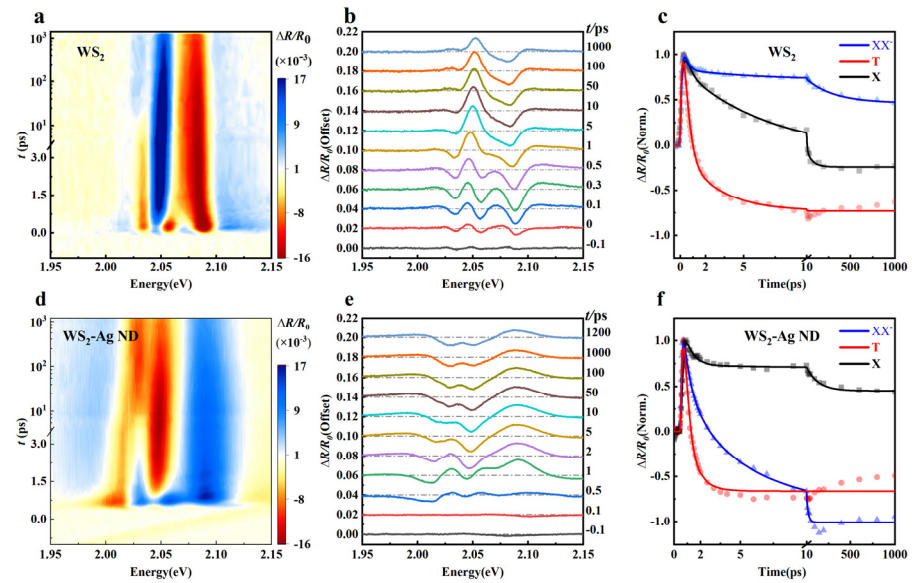


Figure 5. Time-resolved differential reflection spectra of monolayer WS₂ and the WS₂-Ag ND heterostructure at 4K, with a pump fluence of 10 μJ cm⁻². (a,d) A 2D pseudo-color image; red (blue) region denotes the photoinduced bleaching (absorption). (b,e) Transient differential reflection spectra at selected probe delays. (c) Differential reflection kinetics of monolayer WS₂ at three exciton resonances. (f) Differential reflection kinetics of WS₂-Ag ND heterostructure at three exciton resonances.

Here, τ_{rise} represents the ascending process of the kinetic curve, which can be assigned to the formation of three kinds of excitons. After the pulse pumping, hot carriers are generated in the valence and conduction bands. Subsequently, the resulting hot electrons and holes undergo relaxation to the band edge through nonradiative processes like phonon emissions. The large Coulomb interaction between the conduction band bottom electrons and the valence band top holes leads to their coalescence into quasiparticles, marking the creation of exciton, trion, and charged biexciton in the sample. It can be seen that τ_{rise} in the heterostructure region decreases compared with findings in the monolayer WS₂ region, which indicates that the coupling of the plasmonic nanocavity enhances the formation process of exciton, trion, and charged biexciton. The enhancement of this process could stem from the energy transfer prompted by the coherent interplay between plasmon and monolayer WS₂ coupling, or from the injection of hot electrons induced by plasmons. Among the three components of the recovery process, the fastest component (τ_1) can be assigned to the Auger process, the intermediate component (τ_2) can be assigned to the trap-assisted non-radiative recombination process, and the slowest component (τ_3) can be assigned to the radiative recombination process [30]. Unfortunately, the peak signal at the resonant position of the trion is masked after 1 ps due to band renormalization, thus failing to fit the radiative recombination lifetime (τ_3) of the trion. For all of the three exciton complexes, the parameters (including τ_1 , τ_2 and τ_3) in the heterostructure are shorter than those in the controlled WS₂. Such an accelerated relaxation indicates that the coupling of plasmonic nanocavity enhances the excitonic recombination processes. Notably, the radiative recombination lifetime (τ_3) of XX⁻ is drastically shortened by a factor of 15-fold, which is much higher than that of X (~2-fold). Thus, it can be concluded that the promotion effect of plasmonics on the radiative recombination of XX⁻ is much stronger than that on exciton, a finding which is consistent with previous PL analyses. The reduction in the radiative recombination lifetime during the recombination process promotes higher competition in radiation recombination, resulting in an increased proportion of radiation recombination and a significant enhancement in PL intensity.

Phenomenologically, the PL enhancement mechanism of the plasmonic nanocavity relative to excitonic complexes is shown in Figure 6. Firstly, from the prospect of photo absorption, the photoexciting plasmon enhances the generation of exciton via energy

transfer from Ag ND to WS₂, followed by cooling of the hot electrons and holes through phonon emission. Apart from the energy transfer (i.e., both the electron and hole transfer to WS₂), charged transfer (i.e., hot electron transfer to WS₂) is also activated due to the femtosecond pulse pumping, in which the electrons with a high enough kinetic energy can overcome the interface barrier and transfer to WS₂. The charged transfer may lead to efficiently charged doping of the monolayer, resulting in the transition of neutral exciton of the charged excitons (T and XX⁻). Since the emission energy is lowest for XX⁻, most of the transfer energy will be converted into this five-particle state, leading to the drastic enhancement of its population. Secondly, for the recombination process, as discussed above, the plasmon greatly enhances the radiation recombination rates of XX⁻, which may inhibit the non-radiative recombination pathways and enhance the internal quantum efficiency of the PL emission. Combining both the photo absorption and emission factors, the excitonic PL is significantly enhanced in the WS₂-Ag ND heterostructure, particularly for the XX⁻, which possesses the lowest emission energy, serving as an energy reservoir in the hybrid system. Considering all factors, the emission of charged biexciton dominates the heterogeneous region.

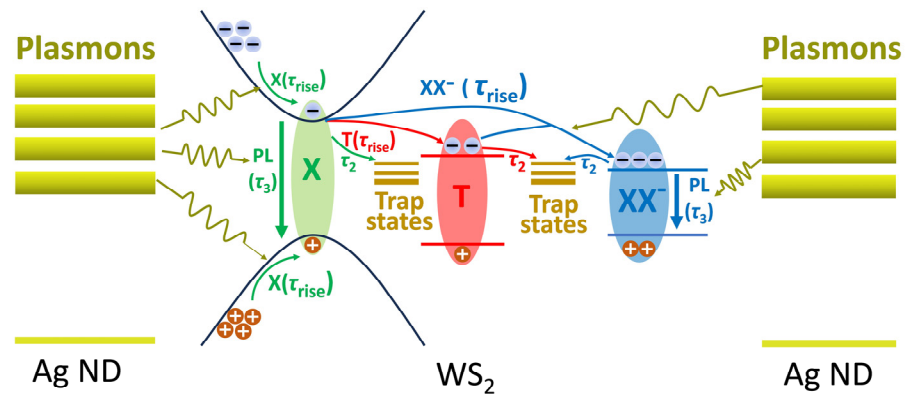


Figure 6. Schematic diagram of the plasmonic effect on the exciton, trion, and charged biexciton dynamics in the WS₂-Ag ND heterostructure. The three colored arrows (green, red, and blue) represent the of exciton, trion and charged biexciton, respectively, including both the formation (τ_{rise}) and the recombination (τ_2 and τ_3) processes, where τ_2 denotes the trap-assisted recombination process, and τ_3 represents the radiation recombination process. The greenish yellow arrow represents the plasmons-enhancement process.

4. Conclusions

The PL enhancement of charged biexciton in monolayer WS₂ coupled with plasmonic nanocavity has been thoroughly investigated. Through steady-state power-dependent PL measurement, we demonstrate the existence of charged biexciton. Notably, we observe a ~114.3-fold enhancement in the charged biexciton PL signal attributed to Fano resonance coupling, significantly surpassing the enhancements seen in both the exciton (~2.2-fold) and trion (~16.4-fold) emissions, a finding which, to our knowledge, had not been observed in previous studies. By applying femtosecond pump-probe measurements, we can clearly observe the change law of multibody exciton states with time, so we successfully established a phenomenological model to clearly analyze the PL enhancement process of charged biexciton in the sample. The effect of plasmonics on the radiative recombination lifetime of charged biexciton (~15-fold) is much stronger than that found with exciton (~2-fold). The establishment of the phenomenological model can not only analyze the details of the enhancement process of charged double excitons, but also provide a valuable point of view for us to understand the coupling between the multibody exciton state and the plasmon cavity in TMD-based materials. This work offers valuable insights into the coupling of the plasmonic nanocavity with high-order excitonic complexes in TMD-based materials, providing a new multi-body exciton pathway for high-performance optical and

photoelectric devices. It establishes a groundwork for, in the future, utilizing charged double excitons as a high-brightness entangled-state light source.

Author Contributions: Conceptualization, H.G. and Y.T.; investigation, H.G. and Q.L.; funding acquisition, K.W. and Y.T.; data curation, H.G. and Q.L.; writing—original draft, H.G. and K.W.; supervision, K.W. All authors have read and agreed to the published version of the manuscript.

Funding: This research was funded by The National Natural Science Foundation of China (62105364, 62075240, 12304353); The Scientific Research Foundation of the National University of Defense Technology (ZK22-16, ZK23-06).

Institutional Review Board Statement: Not applicable.

Informed Consent Statement: Not applicable.

Data Availability Statement: Data underlying the results presented in this paper are not publicly available at this time but may be obtained from the authors upon reasonable request.

Conflicts of Interest: The authors declare no conflicts of interest.

References

- Novoselov, K.S.; Mishchenko, A.; Carvalho, A. 2D Materials and van Der Waals Heterostructures. *Science* **2016**, *353*, aac9439. [[CrossRef](#)] [[PubMed](#)]
- Wang, Q.H.; Kalantar-Zadeh, K.; Kis, A.; Coleman, J.N.; Strano, M.S. Electronics and Optoelectronics of Two-Dimensional Transition Metal Dichalcogenides. *Nat. Nanotechnol.* **2012**, *7*, 699–712. [[CrossRef](#)] [[PubMed](#)]
- Mak, K.F.; Xiao, D.; Shan, J. Light–Valley Interactions in 2D Semiconductors. *Nat. Photonics* **2018**, *12*, 451–460. [[CrossRef](#)]
- Qiu, D.Y.; da Jornada, F.H.; Louie, S.G. Optical Spectrum of MoS₂: Many-Body Effects and Diversity of Exciton States. *Phys. Rev. Lett.* **2013**, *111*, 216805. [[CrossRef](#)] [[PubMed](#)]
- Mostaani, E.; Hunt, R.J.; Thomas, D.M.; Szytniszewski, M.; Montblanch, A.R.-P.; Barbone, M.; Atatüre, M.; Drummond, N.D.; Ferrari, A.C. Charge Carrier Complexes in Monolayer Semiconductors. *Phys. Rev. B* **2023**, *108*, 035420. [[CrossRef](#)]
- Barbone, M.; Montblanch, A.R.-P.; Kara, D.M.; Palacios-Berraquero, C.; Cadore, A.R.; De Fazio, D.; Pingault, B.; Mostaani, E.; Li, H.; Chen, B.; et al. Charge-Tuneable Biexciton Complexes in Monolayer WSe₂. *Nat. Commun.* **2018**, *9*, 3721. [[CrossRef](#)] [[PubMed](#)]
- Paur, M.; Molina-Mendoza, A.J.; Bratschitsch, R.; Watanabe, K.; Taniguchi, T.; Mueller, T. Electroluminescence from Multi-Particle Exciton Complexes in Transition Metal Dichalcogenide Semiconductors. *Nat. Commun.* **2019**, *10*, 1709. [[CrossRef](#)]
- Li, Z.; Wang, T.; Lu, Z.; Jin, C.; Chen, Y.; Meng, Y.; Lian, Z.; Taniguchi, T.; Watanabe, K.; Zhang, S.; et al. Revealing the Biexciton and Trion-Exciton Complexes in BN Encapsulated WSe₂. *Nat. Commun.* **2018**, *9*, 3719. [[CrossRef](#)] [[PubMed](#)]
- Courtade, E.; Semina, M.; Manca, M.; Glazov, M.M.; Robert, C.; Cadiz, F.; Wang, G.; Taniguchi, T.; Watanabe, K.; Pierre, M.; et al. Charged Excitons in Monolayer WSe₂: Experiment and Theory. *Phys. Rev. B* **2017**, *96*, 085302. [[CrossRef](#)]
- Wang, Z.; Dong, Z.; Gu, Y.; Chang, Y.-H.; Zhang, L.; Li, L.-J.; Zhao, W.; Eda, G.; Zhang, W.; Grinblat, G.; et al. Giant Photoluminescence Enhancement in Tungsten-Diselenide–Gold Plasmonic Hybrid Structures. *Nat. Commun.* **2016**, *7*, 11283. [[CrossRef](#)]
- Tugchin, B.N.; Doolaard, N.; Barreda, A.I.; Zhang, Z.; Romashkina, A.; Fasold, S.; Staude, I.; Eilenberger, F.; Pertsch, T. Photoluminescence Enhancement of Monolayer WS₂ by n-Doping with an Optically Excited Gold Disk. *Nano Lett.* **2023**, *23*, 10848–10855. [[CrossRef](#)] [[PubMed](#)]
- Zhang, W.; Gao, L.; Yan, X.; Xu, H.; Wei, H. Excitation and Emission Distinguished Photoluminescence Enhancement in a Plasmon–Exciton Intermediate Coupling System. *Nanoscale* **2023**, *15*, 7812–7819. [[CrossRef](#)] [[PubMed](#)]
- Rozenman, G.G.; Peisakhov, A.; Zadok, N. Dispersion of Organic Exciton Polaritons—A Novel Undergraduate Experiment. *Eur. J. Phys.* **2022**, *43*, 035301. [[CrossRef](#)]
- Sun, J.; Hu, H.; Pan, D.; Zhang, S.; Xu, H. Selectively Depopulating Valley-Polarized Excitons in Monolayer MoS₂ by Local Chirality in Single Plasmonic Nanocavity. *Nano Lett.* **2020**, *20*, 4953–4959. [[CrossRef](#)] [[PubMed](#)]
- Viarbitskaya, S.; Teulle, A.; Marty, R.; Sharma, J.; Girard, C.; Arbouet, A.; Dujardin, E. Tailoring and Imaging the Plasmonic Local Density of States in Crystalline Nanoprisms. *Nat. Mater* **2013**, *12*, 426–432. [[CrossRef](#)] [[PubMed](#)]
- Tang, Y.; Zhang, Y.; Cao, F.; Sui, Y.; Cheng, X.; Shi, L.; Jiang, T. Ultrafast Resonant Exciton–Plasmon Coupling for Enhanced Emission in Lead Halide Perovskite with Metallic Ag Nanostructures. *Opt. Lett.* **2022**, *47*, 3916. [[CrossRef](#)] [[PubMed](#)]
- Cao, E.; Lin, W.; Sun, M.; Liang, W.; Song, Y. Exciton-Plasmon Coupling Interactions: From Principle to Applications. *Nanophotonics* **2018**, *7*, 145–167. [[CrossRef](#)]
- Prodan, E.; Radloff, C.; Halas, N.J.; Nordlander, P. A Hybridization Model for the Plasmon Response of Complex Nanostructures. *Science* **2003**, *302*, 419–422. [[CrossRef](#)]
- Miroshnichenko, A.E.; Flach, S.; Kivshar, Y.S. Fano Resonances in Nanoscale Structures. *Rev. Mod. Phys.* **2010**, *82*, 2257–2298. [[CrossRef](#)]

20. Du, W.; Zhao, J.; Zhao, W.; Zhang, S.; Xu, H.; Xiong, Q. Ultrafast Modulation of Exciton–Plasmon Coupling in a Monolayer WS₂–Ag Nanodisk Hybrid System. *ACS Photonics* **2019**, *6*, 2832–2840. [[CrossRef](#)]
21. Huang, J.; Akselrod, G.M.; Ming, T.; Kong, J.; Mikkelsen, M.H. Tailored Emission Spectrum of 2D Semiconductors Using Plasmonic Nanocavities. *ACS Photonics* **2018**, *5*, 552–558. [[CrossRef](#)]
22. Rafique, M.Z.E.; Basiri, A.; Bai, J.; Zuo, J.; Yao, Y. Ultrafast Graphene-Plasmonic Hybrid Metasurface Saturable Absorber with Low Saturation Fluence. *ACS Nano* **2023**, *17*, 10431–10441. [[CrossRef](#)] [[PubMed](#)]
23. Melendez, L.V.; Van Embden, J.; Connell, T.U.; Duffy, N.W.; Gómez, D.E. Optimal Geometry for Plasmonic Hot-Carrier Extraction in Metal–Semiconductor Nanocrystals. *ACS Nano* **2023**, *17*, 4659–4666. [[CrossRef](#)] [[PubMed](#)]
24. Colin-Ulloa, E.; Fitzgerald, A.; Montazeri, K.; Mann, J.; Natu, V.; Ngo, K.; Uzarski, J.; Barsoum, M.W.; Titova, L.V. Ultrafast Spectroscopy of Plasmons and Free Carriers in 2D MXenes. *Adv. Mater.* **2023**, *35*, 2208659. [[CrossRef](#)] [[PubMed](#)]
25. Zheng, D.; Zhang, S.; Deng, Q.; Kang, M.; Nordlander, P.; Xu, H. Manipulating Coherent Plasmon–Exciton Interaction in a Single Silver Nanorod on Monolayer WSe₂. *Nano Lett.* **2017**, *17*, 3809–3814. [[CrossRef](#)]
26. Fu, S.; du Fossé, I.; Jia, X.; Xu, J.; Yu, X.; Zhang, H.; Zheng, W.; Krasel, S.; Chen, Z.; Wang, Z.M.; et al. Long-Lived Charge Separation Following Pump-Wavelength-Dependent Ultrafast Charge Transfer in Graphene/WS₂ Heterostructures. *Sci. Adv.* **2021**, *7*, eabd9061. [[CrossRef](#)] [[PubMed](#)]
27. Wei, K.; Zheng, X.; Cheng, X.; Shen, C.; Jiang, T. Observation of Ultrafast Exciton–Exciton Annihilation in CsPbBr₃ Quantum Dots. *Adv. Opt. Mater.* **2016**, *4*, 1993–1997. [[CrossRef](#)]
28. Pogna, E.A.A.; Marsili, M.; De Fazio, D.; Dal Conte, S.; Manzoni, C.; Sangalli, D.; Yoon, D.; Lombardo, A.; Ferrari, A.C.; Marini, A.; et al. Photo-Induced Bandgap Renormalization Governs the Ultrafast Response of Single-Layer MoS₂. *ACS Nano* **2016**, *10*, 1182–1188. [[CrossRef](#)] [[PubMed](#)]
29. Wei, K.; Liu, Q.; Tang, Y.; Ye, Y.; Xu, Z.; Jiang, T. Charged Biexciton Polaritons Sustaining Strong Nonlinearity in 2D Semiconductor-Based Nanocavities. *Nat. Commun.* **2023**, *14*, 5310. [[CrossRef](#)] [[PubMed](#)]
30. Chowdhury, R.K.; Nandy, S.; Bhattacharya, S.; Karmakar, M.; Bhaktha, S.N.B.; Datta, P.K.; Taraphder, A.; Ray, S.K. Ultrafast Time-Resolved Investigations of Excitons and Biexcitons at Room Temperature in Layered WS₂. *2D Mater.* **2018**, *6*, 015011. [[CrossRef](#)]

Disclaimer/Publisher’s Note: The statements, opinions and data contained in all publications are solely those of the individual author(s) and contributor(s) and not of MDPI and/or the editor(s). MDPI and/or the editor(s) disclaim responsibility for any injury to people or property resulting from any ideas, methods, instructions or products referred to in the content.